Electronic Supplementary Material (ESI) for Dalton Transactions.

Supplementary Information

Tunable magnetic anisotropy in luminescent cyanido-bridged $\{Dy_2Pt_3\}$ molecules incorporating heteroligand Pt^{IV} linkers

Agnieszka Puzan,[a] Mikolaj Zychowicz,[a] Junhao Wang,[b] Jakub J. Zakrzewski,[a]
Mateusz Reczyński,[a,b] Shin-ichi Ohkoshi,[b,]*and Szymon Chorazy[a,]*

[a]Faculty of Chemistry, Jagiellonian University, Gronostajowa 2, 30-387 Kraków, Poland. [b]Department of Chemistry, School of Science, The University of Tokyo, 7-3-1 Hongo, Bunkyo-ku, Tokyo 113-0033, Japan.

E-mail: ohkoshi@chem.s.u-tokyo.ac.jp (S.O.); chorazy@chemia.uj.edu.pl (S.C.)

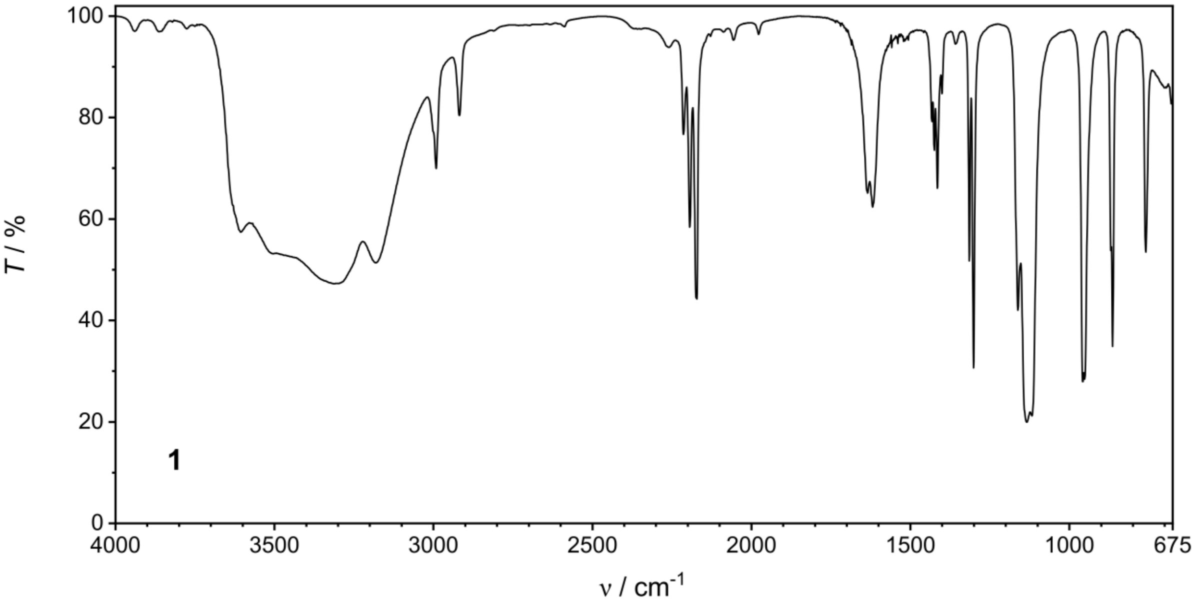

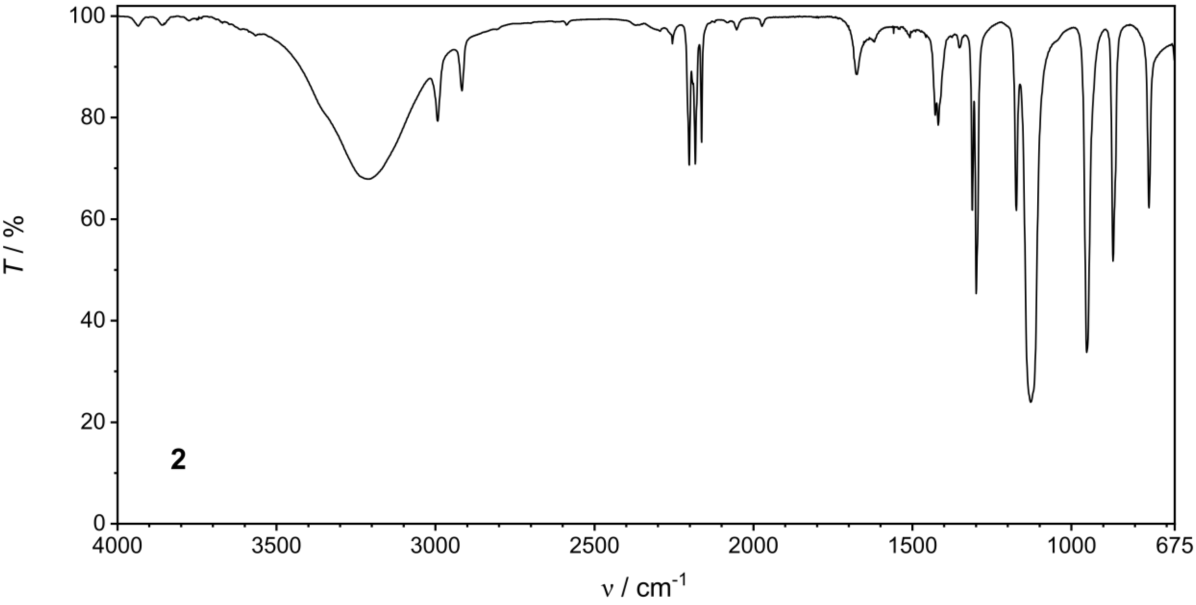

Fig. S1 Infrared (IR) absorption spectra of the selected single crystals of **1** (top) and **2** (bottom) collected in the 4000–675 cm^{-1} wavenumber range.

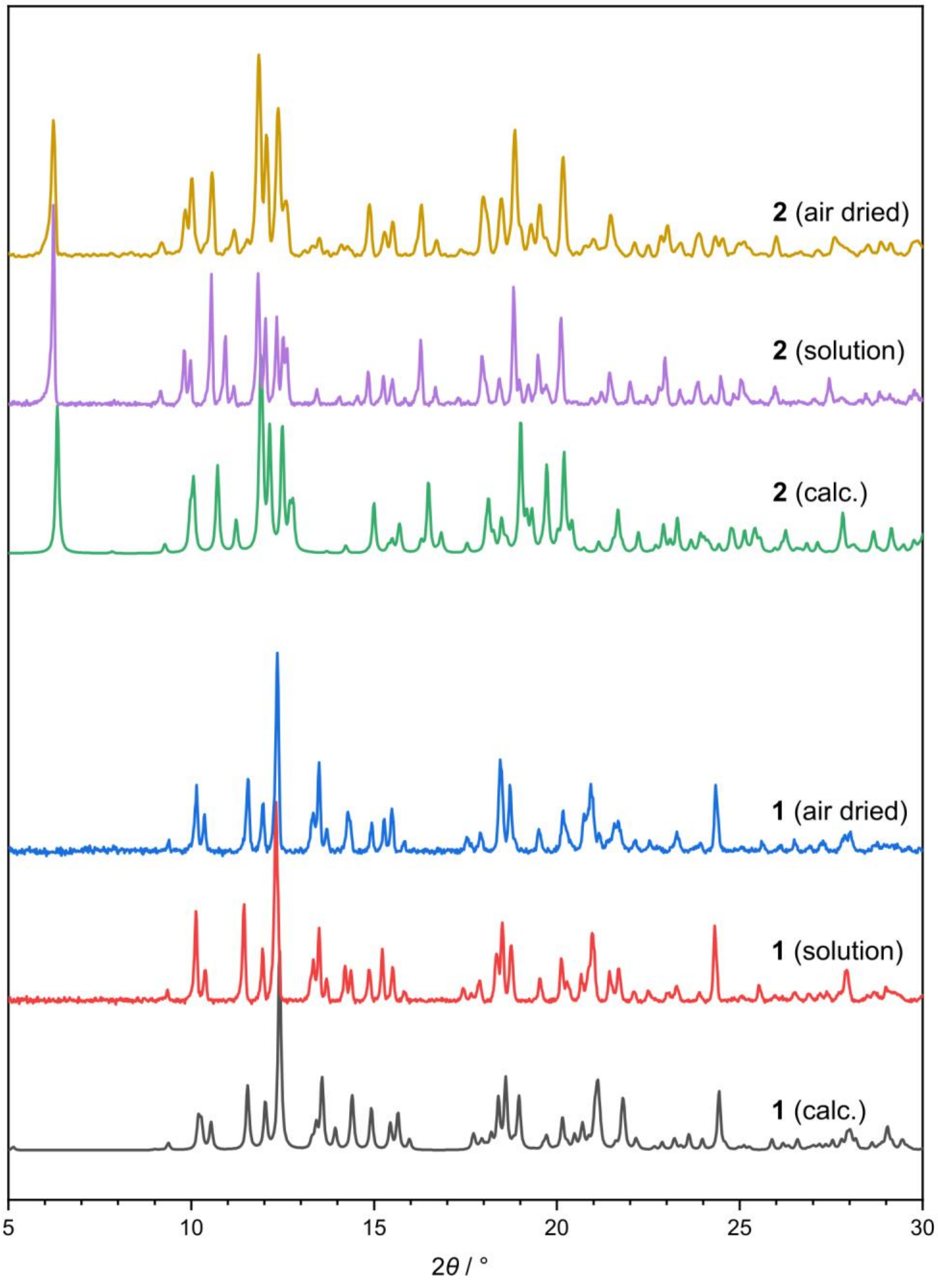

Fig. S2 Powder X-ray diffraction (P-XRD) patterns for the bulk samples of **1** and **2**, including the calculated patterns from the structural models obtained within the single-crystal X-ray diffraction (SC-XRD) analysis (calc., T = 100 K), and experimental (room temperature) P-XRD patterns for the samples placed under the reaction solution (solution) and for the respective air dried samples (air dried). Only the representative range of the 2ϑ angle of 5–30° was presented.

Table S1 Selected crystal data and details of structure refinement for **1**, **2**, and $(TBA)_2[PtBr_2(CN)_4]$.

		1	**2**	$(TBA)_2[PtBr_2(CN)_4]$
				crystal data
formula		$C_{30}H_{70}Br_6Dy_2N_{12}O_{14}P_6Pt_3$	$C_{40}H_{82}Br_6Dy_2N_{14}O_{10}P_8Pt_3$	$C_{36}H_{72}Br_2N_6Pt$
formula weight / g·mol^{-1}		2398.53	2556.68	943.90
radiation type		Mo *K*α radiation, λ = 0.71073 Å		
crystal system		triclinic	monoclinic	monoclinic
space group		$P\bar{1}$	$P2_1/n$	$C2/c$
***T* / K**		100(2)	100(2)	100(2)
cell parameters	***a* / Å**	9.8520(5)	10.0701(5)	48.000(3)
	***b* / Å**	9.9587(6)	22.5477(11)	14.7404(9)
	***c* / Å**	17.7451(10)	18.1808(9)	20.1060(11)
	***α* / °**	75.918(1)	90	90
	***β* / °**	86.751(1)	102.908(2)	114.148(2)
	***γ* / °**	85.387(1)	90	90
***V* / Å^3**		1682.00(16)	4023.8(3)	12987.0(13)
Z		1	2	12
calculated density / g·cm^{-3}		2.368	2.110	1.449
absorption coefficient / mm^{-1}		12.17	10.22	5.12
***F*(000)**		1112	2392	5736
crystal size / mm × mm × mm		0.13 × 0.11 × 0.08	0.06 × 0.05 × 0.04	0.18 × 0.15 × 0.04
				data collection
ϑ range		2.7–27.1°	2.3–27.1°	2.7–26.5°
limiting indices		$h = -12 \rightarrow 12$ $k = -12 \rightarrow 12$ $l = -22 \rightarrow 22$	$h = -12 \rightarrow 12$ $k = -28 \rightarrow 28$ $l = -23 \rightarrow 22$	$h = -60 \rightarrow 60$ $k = -18 \rightarrow 18$ $l = -25 \rightarrow 25$
measured reflections		19791	46593	80328
symmetry–independent reflections		7406	8850	13245
observed reflections [$I > 2\sigma(I)$]		6446	7201	10498
R_{int}		0.028	0.057	0.068
completeness / %		99.6	99.9	95.4
				refinement
refinement method		full-matrix least-squares on F^2		
data / parameters / restrains		7406 / 337 / 12	8850 / 377 / 3	13245 / 668 / 32
GoF on F^2		1.02	1.05	1.04
final *R* indices		$R[F^2 > 2\sigma(F^2)] = 0.025$ $wR(F^2) = 0.050$ $w = 1/[\sigma^2(F_o^2) + (0.0174P)^2 + 4.4068P]$	$R[F^2 > 2\sigma(F^2)] = 0.032$ $wR(F^2) = 0.051$ $w = 1/[\sigma^2(F_o^2) + (0.0105P)^2 + 9.3741P]$ $P = (F_o^2+2F_c^2)/3$	$R[F^2 > 2\sigma(F^2)] = 0.036$ $wR(F^2) = 0.067$ $w = 1/[\sigma^2(F_o^2) + (0.0149P)^2 + 57.9412P]$
largest diff. peak/hole / e·Å^{-3}		1.18/ −1.18	0.88 / −0.91	1.32 / −1.23
CCDC deposition number		2084703	2084704	2084705

Table S2 Selected bond lengths, intermetallic distances (Å) and angles (°) representing the crystal structures of **1** and **2** (*T* = 100 K).

1		**2**	
Pt1–C11	2.011(5)	Pt1–C11	1.997(5)
Pt1–C12	2.021(5)	Pt1–C12	1.999(6)
Pt1–C13	2.008(5)	Pt1–C13	2.026(5)
Pt1–C14	2.027(5)	Pt1–C14	2.016(6)
Pt1–Br11	2.4760(5)	Pt1–Br11	2.4847(6)
Pt1–Br12	2.4796(4)	Pt1–Br12	2.4724(6)
Pt2–C21	2.005(4)	Pt2–C21	2.009(5)
Pt2–C22	2.002(5)	Pt2–C22	2.004(5)
Pt2–Br21	2.4796(4)	Pt2–Br21	2.4820(6)
Dy3–N11	2.538(4)	Dy3–N11	2.500(4)
Dy3–N21	2.541(4)	Dy3–N21	2.502(4)
Dy3–O31[a]	2.252(3)	Dy3–O31[a]	2.251(3)
Dy3–O32[a]	2.240(3)	Dy3–O32[a]	2.237(3)
Dy3–O33[b]	2.412(3)	Dy3–O33[a]	2.261(3)
Dy3–O34[b]	2.491(3)	Dy3–O34[a]	2.272(3)
Dy3–O35[a]	2.259(3)	Dy3–O35[b]	2.332(3)
Dy3–O30[b]	2.422(3)		
Pt1–C11–N11	176.4(4)	Pt1–C11–N11	177.8(5)
Dy3–N11–C11	172.7(4)	Dy3–N11–C11	171.6(4)
Pt2–C21–N21	178.4(4)	Pt2–C21–N21	176.2(5)
Dy3–N21–C21	176.6(4)	Dy3–N21–C21	160.7(4)
N11–Dy3–N21	129.32(12)	N11–Dy3–N21	134.90(14)
O31–Dy3–O32	104.15(13)	O31–Dy3–O32	104.35(13)
N11–Dy3–O31	74.38(12)	N11–Dy3–O31	74.50(13)
N11–Dy3–O32	75.48(12)	N11–Dy3–O32	83.48(14)
N21–Dy3–O31	76.28(12)	N21–Dy3–O31	72.22(13)
N21–Dy3–O32	72.88(12)	N21–Dy3–O32	76.32(14)
O31–Dy3–O35	88.20(12)	O31–Dy3–O33	126.79 (13)
O32–Dy3–O35	144.46(12)	O31–Dy3–O34	146.84 (12)
		O32–Dy3–O33	105.61 (14)
		O32–Dy3–O34	82.68 (13)

		O33–Dy3–O34	80.09 (12)
N11–Dy3–O35	85.54(13)	N11–Dy3–O33	151.44 (13)
N21–Dy3–O35	118.31 (13)	N11–Dy3–O34	74.21 (13)
		N21–Dy3–O33	73.56 (13)
		N21–Dy3–O34	140.06 (13)
Pt1···Dy3	5.6673(3)	Pt1···Dy3	5.6244(4)
Pt2···Dy3	5.6892(3)	Pt2···Dy3	5.5419(3)
Pt1···Pt2	9.9645(4)	Pt1···Pt2	9.8729(4)
Dy3···Dy3$^{\mathrm{i}}$	11.3783(7)	Dy3···Dy3$^{\mathrm{i}}$	11.0839(6)
Pt1···Dy3···Pt2	122.667(4)	Pt1···Dy3···Pt2	124.296(5)

The O atoms coordinated to the Dy3 centre originate either from the tmpo ligands (*a*) or water molecules (*b*). The enlisted O/N–Dy3–O angles correspond only to the O atoms originating from the tmpo ligands.

Symmetry codes: (i) −*x*, −*y*+1, −*z*+1.

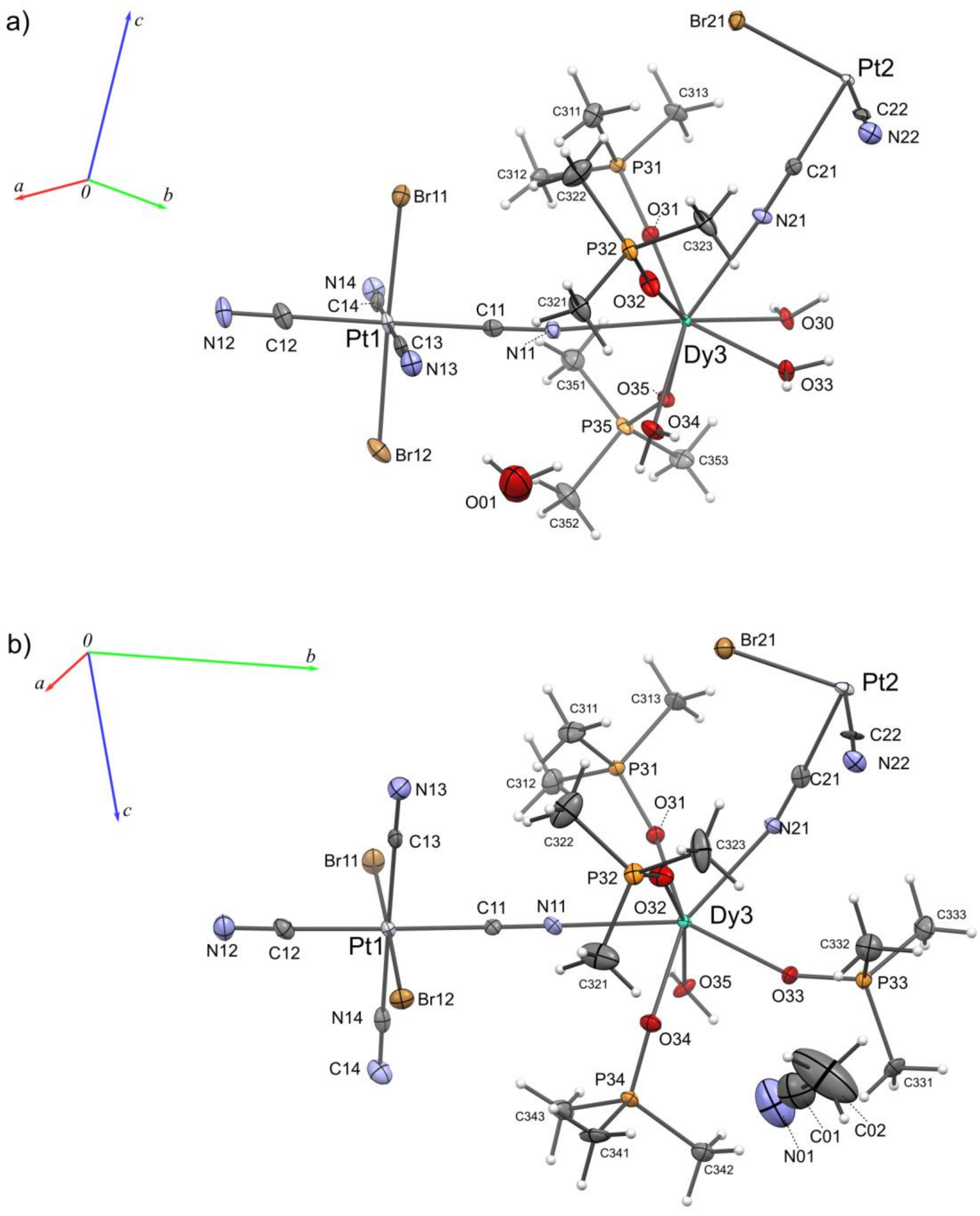

Fig. S3 Asymmetric units of **1** (a) and **2** (b) with the atoms labelling scheme. The thermal ellipsoids are drawn at 40% of the probability level.

Table S3 Continuous Shape Measurement (CShM) parameters for the coordination polyhedrons of metal centres in **1** and **2**.

	CShM[a]				
	Pt1	Pt2	Dy3		
1	OC-6[b]		TDD-8	SAPR-8	BTPR-8
	1.036	1.077	0.870	1.407	1.969
2	OC-6		COC-7	CTPR-7	PBPY-7
	1.047	1.079	1.367	1.691	4.026

a) CShM = 0 corresponds to ideal geometry;

b) OC-6 – octahedron (O_h), COC-7 – capped octahedron (C_{3v}), CTPR-7 – capped trigonal prism (C_{2v}), PBPY-7 – pentagonal bipyramid (D_{5h}), TDD-8 – triangular dodecahedron (D_{2d}), SAPR-8 – square antiprism (D_{4d}), BTPR-8 – biaugmented trigonal prism (C_{2v}).

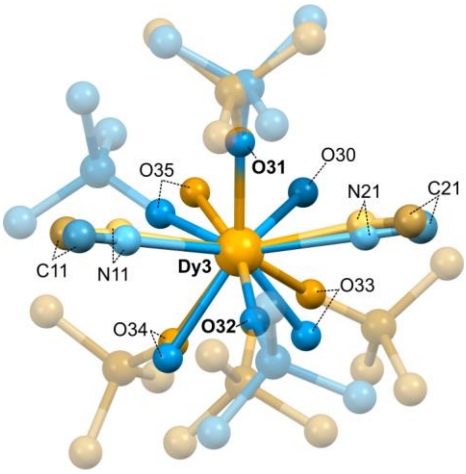

Fig. S4 The comparison of the coordination environment of Dy^{III} centres in **1** (blue) and **2** (orange). The view was obtained by overlaying the Dy3, O31, and O32 atoms, thus the structural differences are emphasized by the positions of other atoms.

Table S4 Hydrogen bonds geometry (Å, °) in the crystal structures of **1** and **2**.

D*—H···*A	***D*—H / Å**	**H···*A* / Å**	***D*···*A* / Å**	***D*—H···*A* / °**
				1
O30—H30*A*···N12^{ii}	0.83	2.70	3.215(5)	121
O30—H30*B*···N13^{iii}	0.84	1.98	2.809(5)	174
O33—H33*A*···N12^{ii}	0.84	2.09	2.894(5)	162
O33—H33*B*···N14^{iv}	0.84	2.18	2.954(5)	154
O34—H34*A*···N14^{iv}	0.83	2.20	3.008(5)	165
O34—H34*B*···O01^{v}	0.83	2.00	2.805(7)	163
O01—H01*A*···Br12	0.88(2)	2.54(4)	3.329(6)	150(7)
O01—H01*B*···O34	0.88(2)	1.95(2)	2.826(6)	172(7)
				2
O35—H35*A*···N22^{vi}	0.83	1.94	2.758(5)	168
O35—H35*B*···N12^{vii}	0.83	1.95	2.783(6)	175

Symmetry codes: (ii) *x*−1, *y*+1, *z*; (iii) *x*−1, *y*, *z*; (iv) *x*, *y*+1, *z*; (v) −*x*+1, −*y*+1, -*z*; (vi) *x*+1, *y*, *z*; (vii)

Table S5 Metric parameters of halogen bonding in crystal structures of **1** and **2**.

R1—X1···X2—R2	**X···X / Å**	**R1—X1···X2 / °**	**R2—X2···X1 / °**	**Type**[1, 2]
				1
Pt1–Br11···Br21^{viii}–Pt2^{viii}	3.4703(7)	119.86(2)	171.88(2)	type II
				2
Pt2–Br21···Br12^{ix}–Pt1^{ix}	3.4714(8)	124.36(2)	165.35(2)	type II

Symmetry codes: (viii) −*x*+1, −*y*, −*z*+1; (ix) *x*−1/2, −*y*+1/2, *z*−1/2.

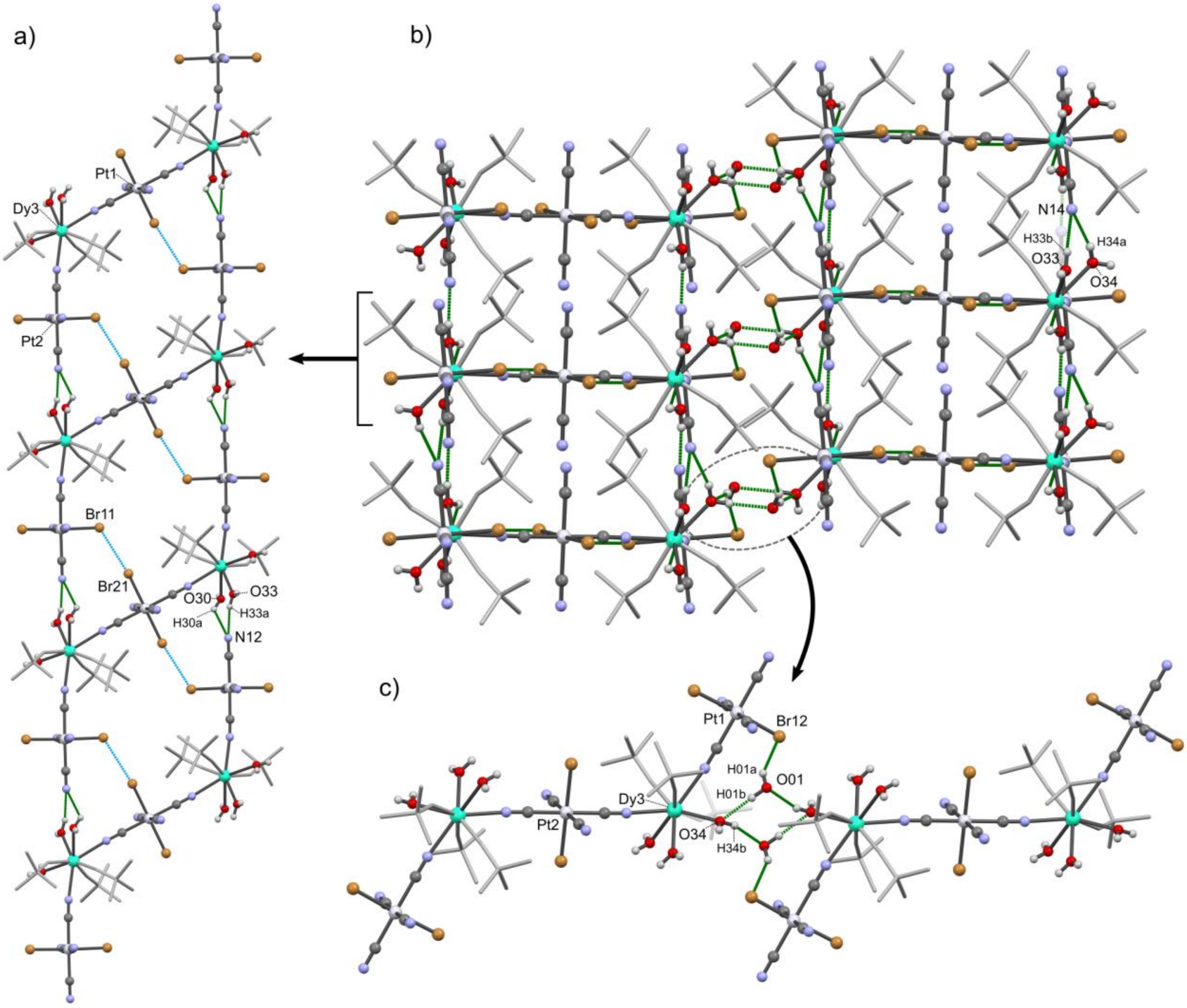

Fig. S5 The representative views of hydrogen bonds (green) and halogen Br···Br bonds (blue) in the crystal structure of **1**: (a) supramolecular ribbons viewed perpendicular to the (110) plane, (b) stacks of the supramolecular ribbons viewed along the [−110] direction, and (c) H-bonds mediated by the crystallisation water molecules.

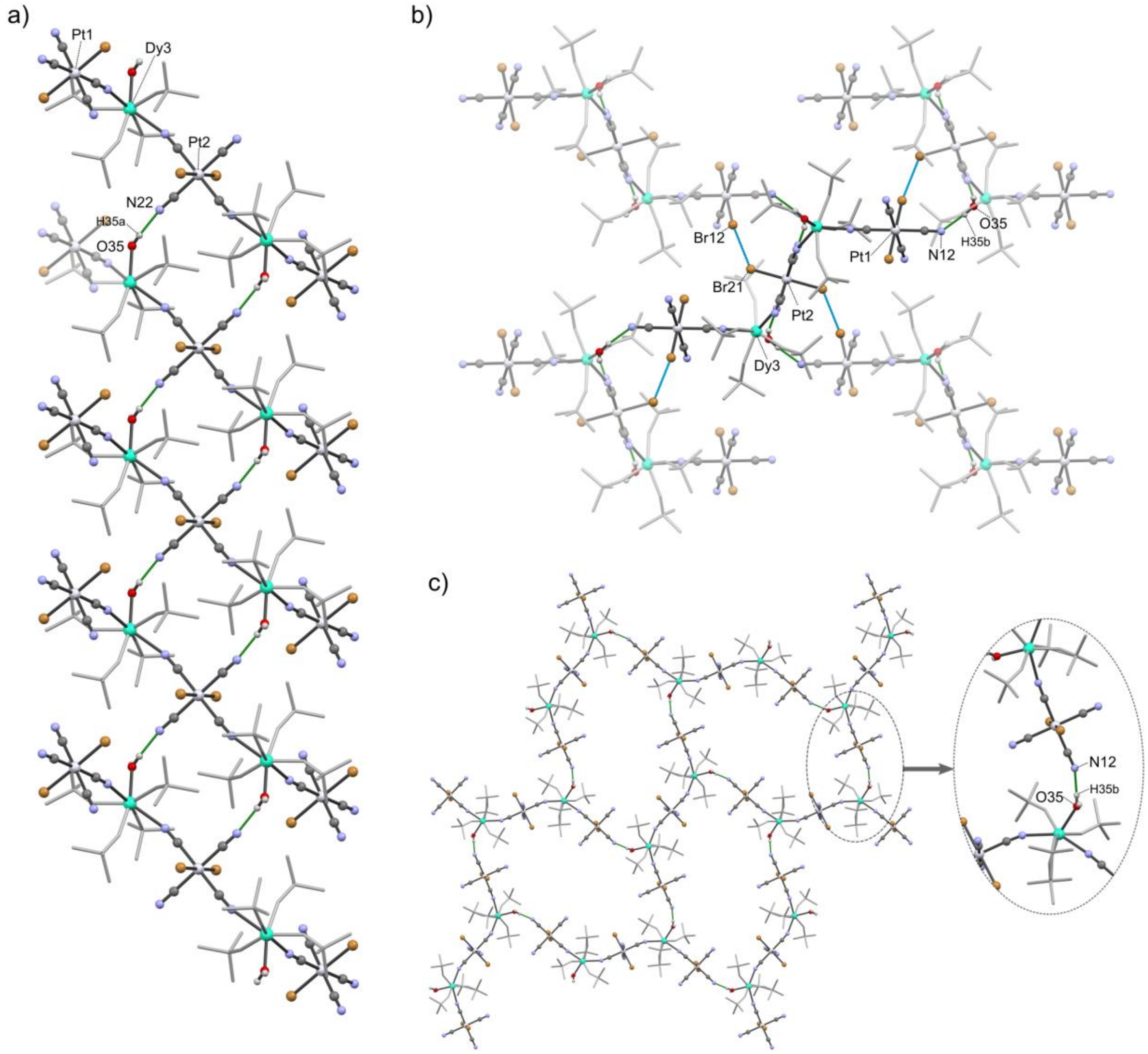

Fig. S6 The representative views of hydrogen bonds (green) and halogen Br···Br bonds (blue) in the crystal structure of **2**: (a) the chains of the H-bonded {Dy_2Pt_3} molecules, (b) and (c) the honeycomb-like motifs of molecules' arrangement.

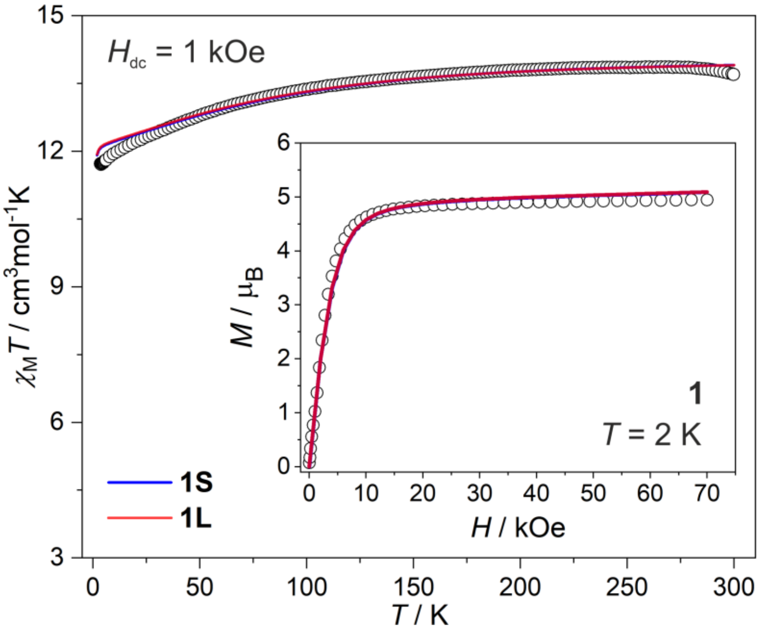

Fig. S7 Direct-current (*dc*) magnetic characteristics of **1**: temperature dependence of the $\chi_M T$ product under the external magnetic field of H_{dc} = 1000 Oe (black circles), field dependence of molar magnetization (M) at T = 2 K (the inset), together with the theoretical curves (solid lines), obtained using the *ab initio* calculations (using two different models, **1S** and **1L**) displayed for the comparison with the experimental ones.

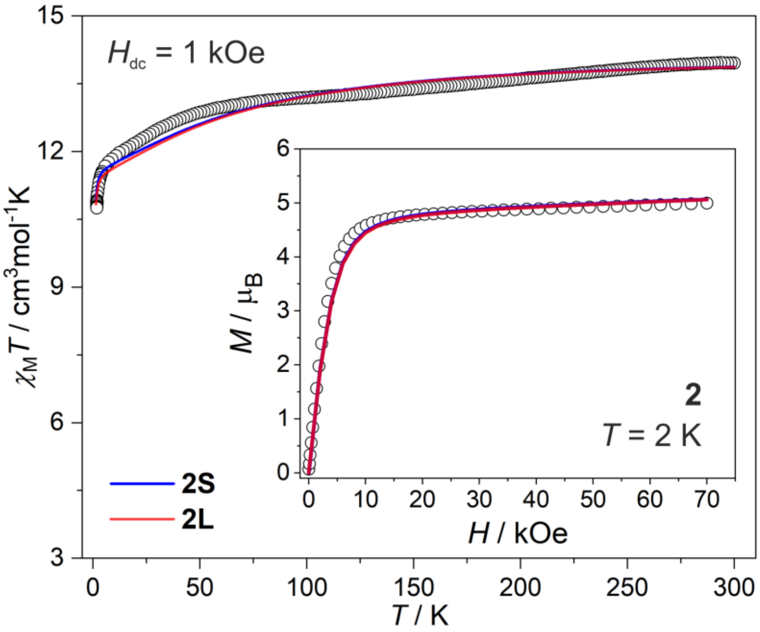

Fig. S8 Direct-current (*dc*) magnetic characteristics of **2**: temperature dependence of the $\chi_M T$ product under the external magnetic field of H_{dc} = 1000 Oe (black circles), field dependence of molar magnetization (M) at T = 2 K (the inset), together with the theoretical curves (solid lines), obtained using the *ab initio* calculations (using two different models, **1S** and **1L**) displayed for the comparison with the experimental ones.

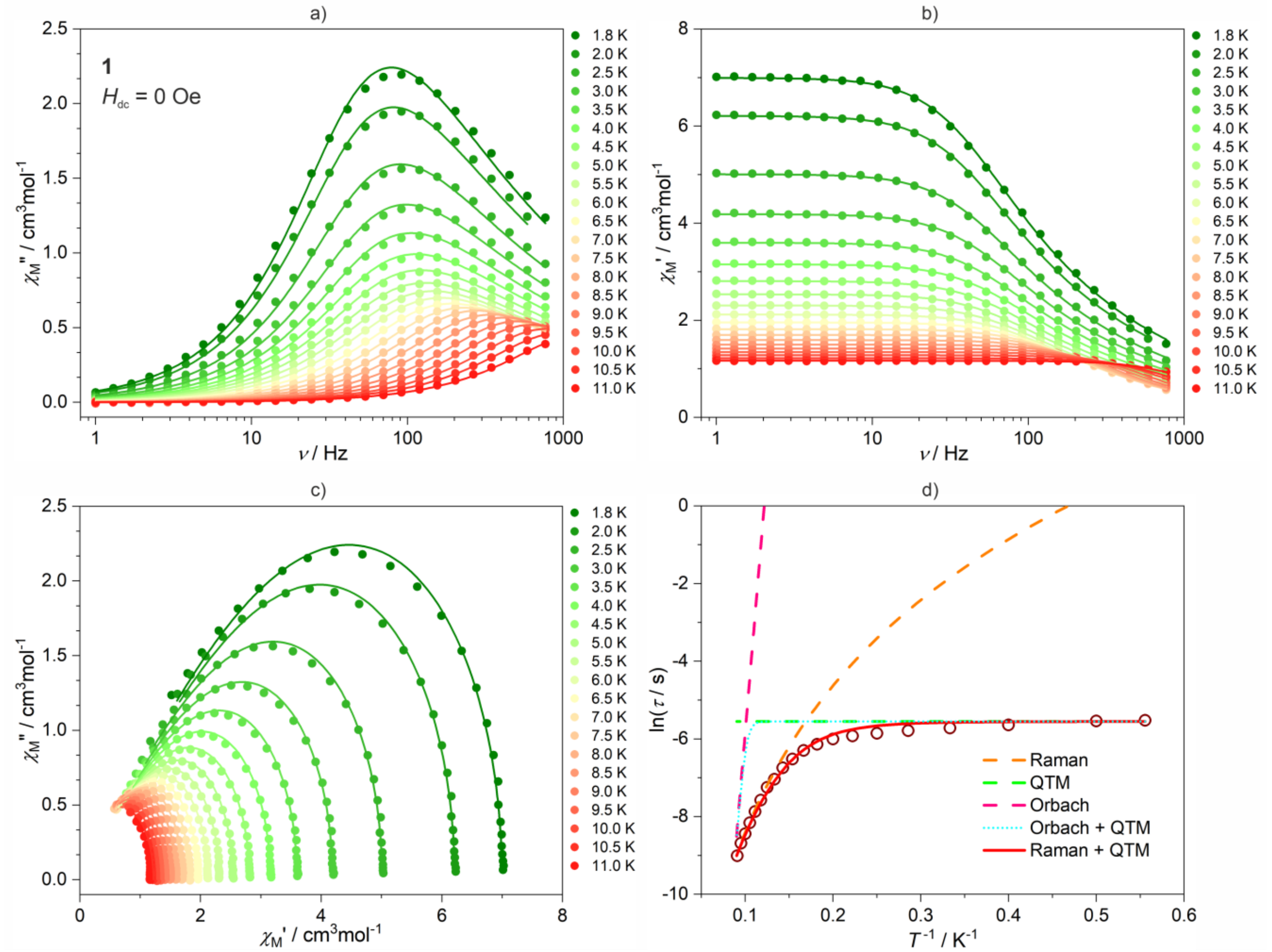

Fig. S9 Complete set of temperature-dependent alternate-current (*ac*) magnetic characteristics of **1** at the zero *dc* field: frequency dependences of χ_M” (a) and χ_M’ (b) at various temperatures in the range of 1.8–11.0 K, together with the respective Argand plots (c), and the temperature dependence of relaxation time plotted as ln(τ) vs. T^{-1} (d). Solid lines in the (a), (b) and (c) parts represent the best fits to the Cole-Davidson model while the red solid line in (d) shows the result of the fitting of the $\tau(T,H)$ dependency to the Eq. 1 (main text). The orange and green dashed lines represent the resulting contributions of given relaxation processes (Raman and QTM). The related best-fit parameters are gathered in Table 1. The light blue dotted line shows the alternative fitting taking into account the Orbach relaxation along with the QTM when taking into account the thermal energy barrier from the results of the *ab initio* calculations, the pink dashed line represents this Orbach contribution. This alternative is shown for the comparison to underline the lack of Orbach relaxation in the investigated temperature range.

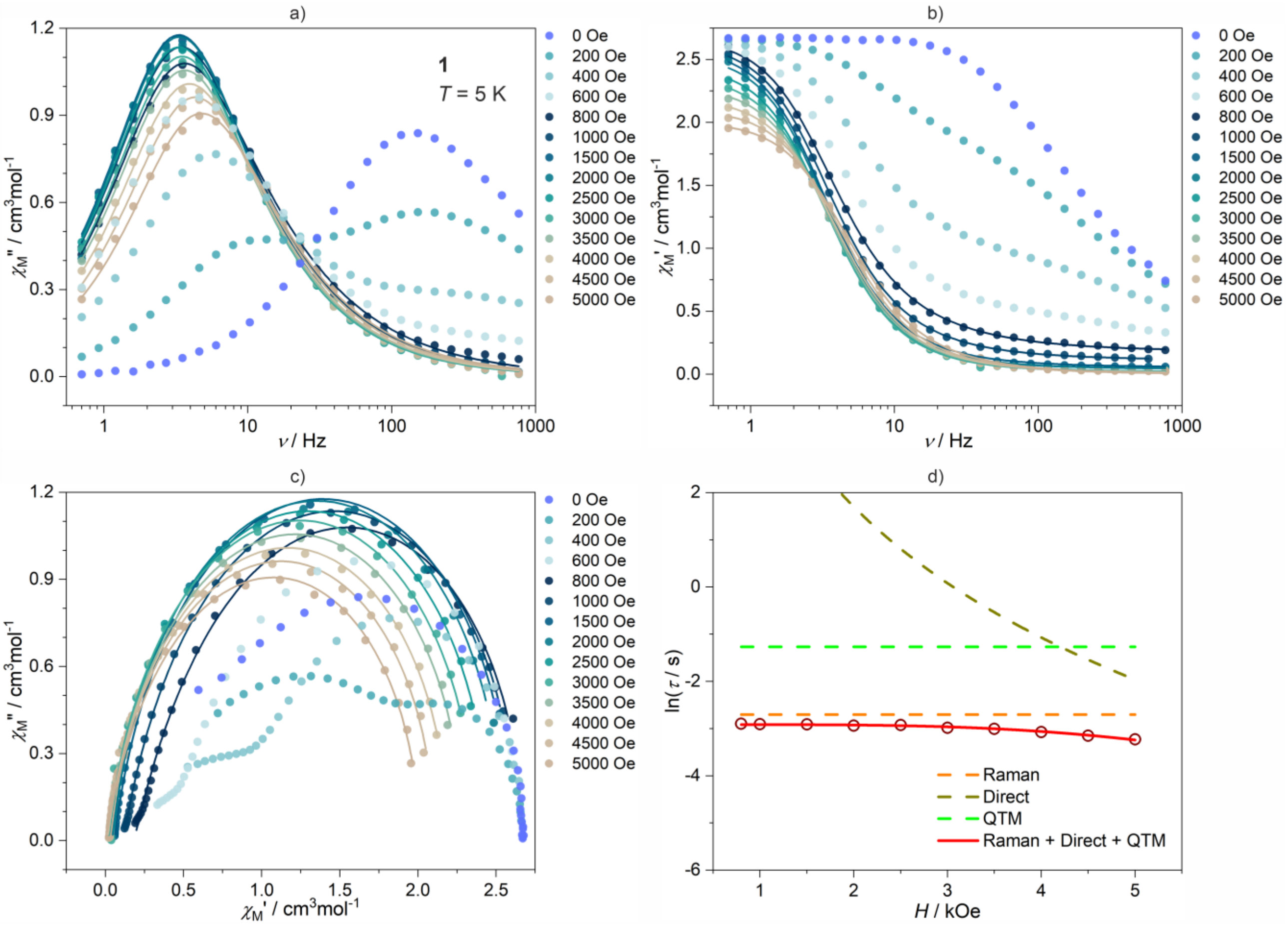

Fig. S10 Complete set of field-variable alternate-current (*ac*) magnetic characteristics of **1** at 5 K: frequency dependences of χ_M'' (a) and χ_M' (b) at various *dc* fields in the range of 0–5000 Oe, together with the respective Argand plots (c), and the field dependence of relaxation time plotted as ln(τ) vs. *H* (d). Solid lines in the (a), (b) and (c) parts represent the best fits to the Cole-Davidson model while the red solid line in (d) shows the result of the fitting of the $\tau(T,H)$ dependency to the Eq. 1 (main text). The coloured dashed lines represent the resulting contributions of given relaxation processes (Raman, Direct, and QTM). The related best-fit parameters are gathered in Table 1.

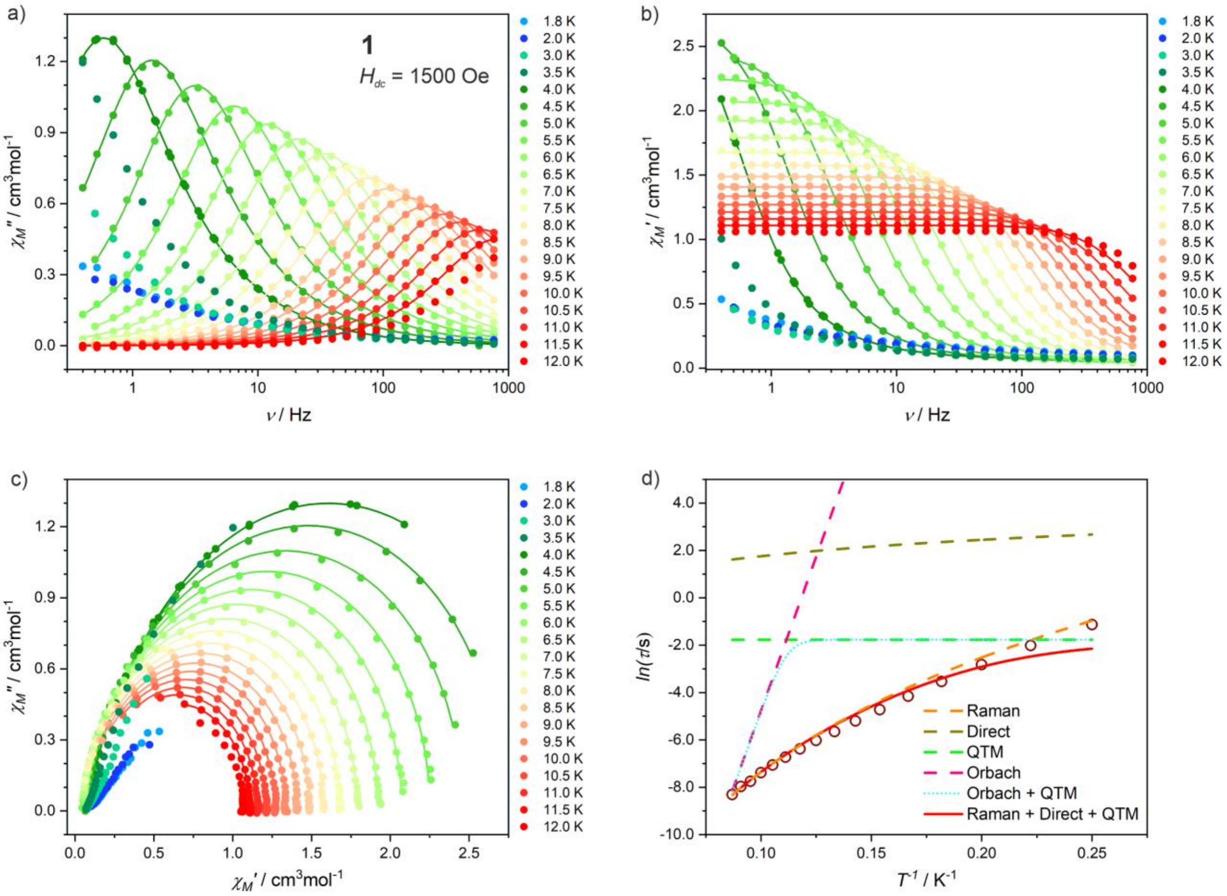

Fig. S11 Complete set of temperature-dependent alternate-current (*ac*) magnetic characteristics of **1** at the optimal *dc* field of 1.5 kOe: frequency dependences of χ_M'' (a) and χ_M' (b) at various temperatures in the range of 1.8–12.0 K, together with the respective Argand plots (c), and the temperature dependence of relaxation time plotted as ln(τ) vs. T^{-1} (d). Solid lines in the (a), (b) and (c) parts represent the best fits to the Cole-Davidson model while the red solid line in (d) shows the result of the fitting of the $\tau(T,H)$ dependency to the Eq. 1 (main text). The orange, dark green, and light green dashed lines represent the resulting contributions of given relaxation processes (Raman, Direct, and QTM). The related best-fit parameters are gathered in Table 1. The light blue dotted line shows the alternative fitting taking into account the Orbach relaxation along with the QTM when taking into account the thermal energy barrier from the results of the *ab initio* calculations, the pink dashed line represents this Orbach contribution. This alternative is shown for the comparison to underline the lack of Orbach relaxation in the investigated temperature range.

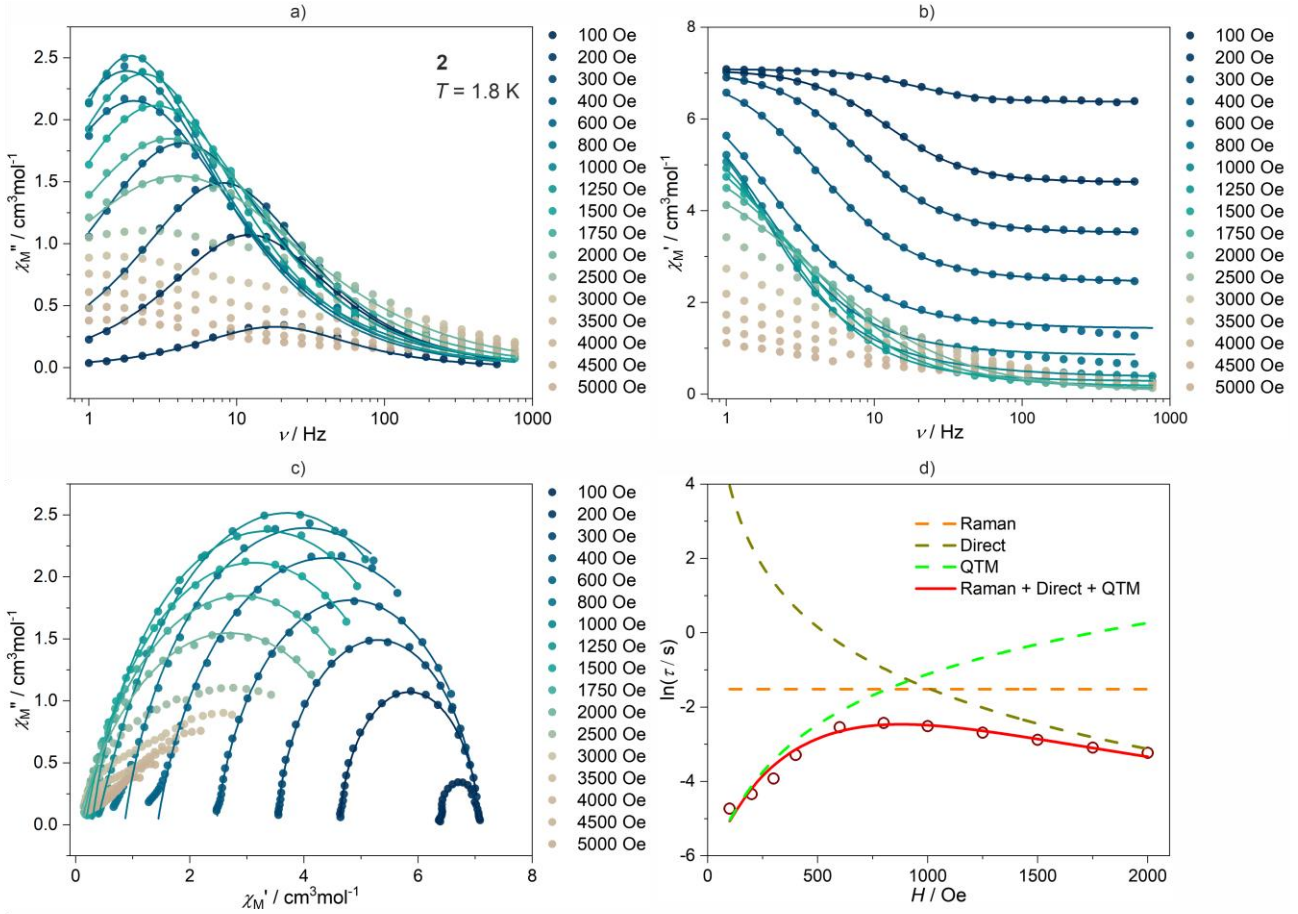

Fig. S12 Complete set of field-variable alternate-current (*ac*) magnetic characteristics of **2** at 1.8 K: frequency dependences of χ_M'' (a) and χ_M' (b) at various *dc* fields in the range of 100–5000 Oe, together with the respective Argand plots (c), and the field dependence of relaxation time plotted as ln(τ) vs. H (d). Solid lines in the (a), (b) and (c) parts represent the best fits to the generalized Debye model while the red solid line in (d) shows the result of the fitting of the $\tau(T,H)$ dependency to the Eq. 1 (main text). The coloured dashed lines represent the resulting contributions of given relaxation processes (Raman, Direct, and QTM). The related best-fit parameters are gathered in Table 1.

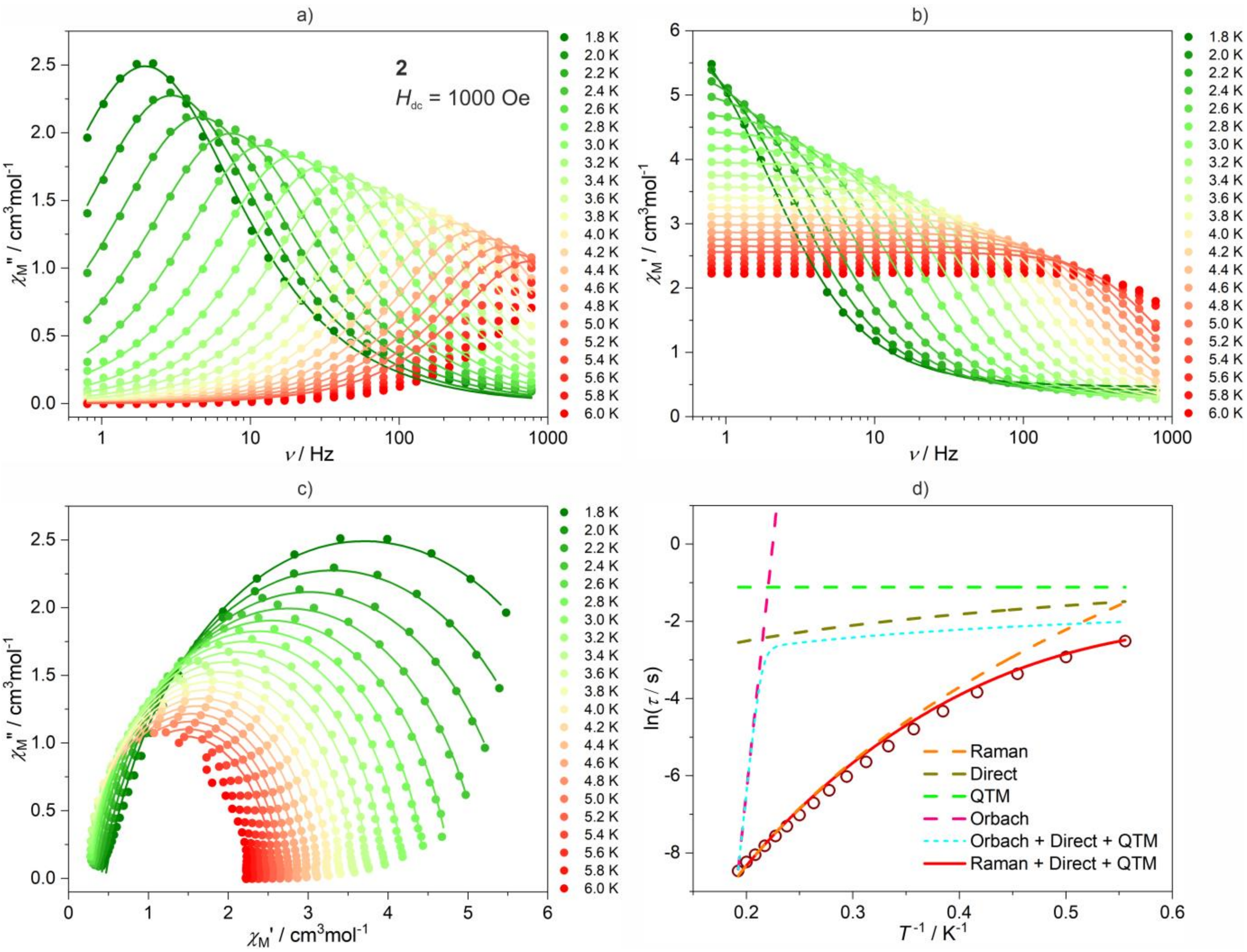

Fig. S13 Complete set of temperature-dependent alternate-current (*ac*) magnetic characteristics of **2** at the optimal *dc* field of 1 kOe: frequency dependences of χ_M" (a) and χ_M' (b) at various temperatures in the range of 1.8–6.0 K, together with the respective Argand plots (c), and the temperature dependence of relaxation time plotted as ln(τ) vs. T^{-1} (d). Solid lines in the (a), (b) and (c) parts represent the best fits to the generalized Debye model while the red solid line in (d) shows the result of the fitting of the $\tau(T,H)$ dependency to the Eq. 1 (main text). The orange, dark green, and light green dashed lines represent the resulting contributions of given relaxation processes (Raman, Direct, and QTM). The related best-fit parameters are gathered in Table 1. The light blue dotted line shows the alternative fitting taking into account the Orbach relaxation along with the Direct and QTM relaxation pathways when taking into account the thermal energy barrier from the results of the *ab initio* calculations, the pink dashed line represents this Orbach contribution. This alternative is shown for the comparison to underline the lack of Orbach relaxation in the investigated temperature range.

Comment to Figures S9–S13

To fit the frequency dependences *ac* magnetic susceptibilities, χ_M' and χ_M'' of **1** and **2** (Fig. S9–S13), the Havriliak-Negami model for a single relaxation process was used (Eqn. S1):

$$\chi(\omega) = \chi_S + \frac{(\chi_T - \chi_S)}{(1+(i\omega\tau)^{1-\alpha})^{\beta}} \qquad \text{(S1)}$$

then χ_M' and χ_M'' are expressed as real and imaginary parts of the complex susceptibility:

$$\chi'(\omega) = \mathrm{Re}(\chi_S + \frac{(\chi_T - \chi_S)}{(1+(i\omega\tau)^{1-\alpha})^{\beta}}) \qquad \text{(S2)}$$

$$\chi''(\omega) = -\mathrm{Im}(\chi_S + \frac{(\chi_T - \chi_S)}{(1+(i\omega\tau)^{1-\alpha})^{\beta}}) \qquad \text{(S3)}$$

where

χ_S – the adiabatic susceptibility (at the infinitely high frequency of *ac* field),

χ_T – the isothermal susceptibility (at the infinitely low frequency of *ac* field),

τ – the relaxation time,

and ω is an angular frequency, that is $\omega = 2\pi\nu$, with ν being the linear frequency in [Hz] units.

To avoid over-parameterization, for **1** we set $\alpha = 0$ recreating Cole-Davidson (CD) model, whereas $\beta = 1$ for **2** ending with generalized Debye (GD) model (Cole-Cole model). The choice of a particular expression was made by fitting experimental data with both of them and taking one characterized with the better goodness of fit. Physically, the shape of investigated dependences, especially visible for the Cole-Cole plots, and what follows the distribution of relaxation times, decides which model better recreates the data. In the case of GD, signals of χ_M'', χ_M', and what follows for the Argand diagram, are symmetrical indicating even smearing of the distribution of relaxation times around the single relaxation time τ_c value at the position of χ_M'' maximum. While in the CD model, the distribution of relaxation times is non-symmetrical suggesting the occurrence of an upper limit (cut-off) for relaxation times from which it falls creating a long tail up to the low values of τ.[3]

Table S6 Description and contractions of the basis sets of two different models, **S** – smaller and **L** – larger, employed in the *ab initio* calculations of the Dy^{III} crystal field in **1** and **2**.

Basis set "S"	**Basis set "L"**
Dy.ANO-RCC-VDZP 7S6P4D2F1G	Dy.ANO-RCC-VTZP 8S7P5D3F2G1H
N.ANO-RCC-VDZ 3S2P	N.ANO-RCC-VDZP 3S2P1D (1st coordination sphere) N.ANO-RCC-VDZ 3S2P (others)
O.ANO-RCC-VDZ 3S2P	O.ANO-RCC-VDZP 3S2P1D
C.ANO-RCC-VDZ 3S2P	C.ANO-RCC-VDZ 3S2P
H.ANO-RCC-VDZ 2S	H.ANO-RCC-VDZ 2S
Br.ANO-RCC-VDZ 5S4P1D	Br.ANO-RCC-VDZ 5S4P1D
Pt.ANO-RCC-VDZ 7S6P4D1F	Pt.ANO-RCC-VDZ 7S6P4D1F
P.ANO-RCC-VDZ 4S3P	P.ANO-RCC-VDZ 4S3P

Table S7 Summary of the energy splitting of the $^{6}H_{15/2}$ multiplet of Dy^{III} centers in **1**, calculated using two different models (**S** and **L**) gathered together with related pseudo-*g*-tensors for all Kramers doublets of the ground multiplet and the compositions of two lowest lying doublets in the $|m_J\rangle$ basis.

model S				model L			
energy and pseudo-*g*-tensor components (g_x, g_y, g_z) of 8 ground Kramers doublets							
energy / cm^{-1}	pseudo-*g*-tensor components			energy / cm^{-1}	pseudo-*g*-tensor components		
	g_x	g_y	g_z		g_x	g_y	g_z
0.000	**0.0027**	**0.0040**	19.6536	**0.000**	**0.0022**	**0.0036**	19.6748
180.611	**0.0599**	**0.0674**	16.6253	**179.067**	**0.0456**	**0.0526**	16.6915
297.984	0.8064	2.1903	11.9599	297.879	0.6045	1.8032	12.4364
325.004	0.7142	4.2892	12.7454	329.457	1.2754	4.5466	12.9387
368.056	2.9833	5.3409	9.8543	374.896	0.3099	4.8795	9.9654
392.416	1.3075	3.0202	10.5280	405.428	2.3378	4.3307	9.1942
422.884	0.4797	1.9564	16.8303	430.677	0.8848	3.5071	15.9783
503.009	0.0279	0.0473	19.5011	520.457	0.0302	0.0565	19.5342

model S	model L
composition of the two ground Kramers doublets in the $|m_J\rangle$ basis on the quantization axes within *J* = 15/2 manifold	
1st doublet	**1st doublet**
79.2% $|+15/2\rangle$ 16.8% $|-15/2\rangle$ 3.1% $|+11/2\rangle$ 0.7% $|-11/2\rangle$ 0.1% $|+9/2\rangle$	71.2% $|+15/2\rangle$ 25.3% $|-15/2\rangle$ 2.3% $|+11/2\rangle$ 0.8% $|-11/2\rangle$ 0.1% $|-9/2\rangle$
2nd doublet	**2nd doublet**
78.0% $|+13/2\rangle$ 11.0% $|-13/2\rangle$ 8.0% $|+9/2\rangle$ 1.2% $|+11/2\rangle$ 1.1% $|-9/2\rangle$ 0.2% $|+7/2\rangle$ 0.2% $|+5/2\rangle$ 0.1% $|-3/2\rangle$	89.1% $|+13/2\rangle$ 7.4% $|+9/2\rangle$ 1.5% $|+11/2\rangle$ 1.1% $|-13/2\rangle$ 0.4% $|+7/2\rangle$ 0.2% $|+5/2\rangle$ 0.1% $|+3/2\rangle$ 0.1% $|-9/2\rangle$

Table S8 Summary of the energy splitting of the $^6H_{15/2}$ multiplet of Dy^{III} centers in **2**, calculated using two different models (**S** and **L**) gathered together with related pseudo-*g*-tensors for all Kramers doublets of the ground multiplet and the compositions of two lowest lying doublets in the $|m_J\rangle$ basis.

model S				**model L**			
energy and pseudo-*g*-tensor components (g_x, g_y, g_z) of 8 ground Kramers doublets							
energy / cm^{-1}	pseudo-*g*-tensor components			energy / cm^{-1}	pseudo-*g*-tensor components		
	g_x	g_y	g_z		g_x	g_y	g_z
0.000	**0.1228**	**0.2790**	19.1980	**0.000**	**0.1434**	**0.3406**	19.1002
144.085	**1.3723**	**2.4335**	14.7016	**139.125**	**1.4865**	**2.6498**	14.4395
248.276	4.8196	5.6195	8.0461	244.687	4.9796	5.6597	7.7192
307.616	1.2613	2.0481	15.6141	320.740	0.9870	2.1059	13.5401
361.224	0.0412	0.4957	14.9118	376.332	0.1162	0.4581	15.8300
463.706	0.4935	0.6980	15.9074	476.942	0.5742	1.0147	14.5949
480.323	0.9257	0.9992	16.5094	491.830	0.5701	1.5890	16.8867
501.653	0.0286	0.8546	17.2439	517.462	0.0692	0.3486	18.3301
composition of the two ground Kramers doublets in the $\vert m_J\rangle$ basis on the quantization axes within *J* = 15/2 manifold							
1st doublet				**1st doublet**			
86.6% $\vert +15/2\rangle$ 6.0% $\vert +11/2\rangle$ 4.0% $\vert -15/2\rangle$ 1.5% $\vert +7/2\rangle$ 0.8% $\vert +9/2\rangle$ 0.3% $\vert -11/2\rangle$ 0.3% $\vert +3/2\rangle$ 0.2% $\vert +13/2\rangle$ 0.1% $\vert -7/2\rangle$ 0.1% $\vert -1/2\rangle$				75.3 % $\vert +15/2\rangle$ 13.8 % $\vert -15/2\rangle$ 6.4% $\vert +11/2\rangle$ 1.4% $\vert +7/2\rangle$ 1.2% $\vert -11/2\rangle$ 0.6% $\vert +9/2\rangle$ 0.4% $\vert +3/2\rangle$ 0.3% $\vert -7/2\rangle$ 0.2% $\vert -9/2\rangle$ 0.2% $\vert +13/2\rangle$ 0.1% $\vert -5/2\rangle$ 0.1% $\vert -3/2\rangle$ 0.1% $\vert -1/2\rangle$			
2nd doublet				**2nd doublet**			
55.1% $\vert +13/2\rangle$ 12.0% $\vert +9/2\rangle$ 9.6% $\vert -13/2\rangle$ 7.8% $\vert +5/2\rangle$ 3.9% $\vert +7/2\rangle$ 2.6 % $\vert -9/2\rangle$ 2.3% $\vert +1/2\rangle$ 1.5% $\vert -5/2\rangle$ 1.4% $\vert +11/2\rangle$ 0.9% $\vert -3/2\rangle$ 0.7% $\vert -1/2\rangle$ 0.6% $\vert -7/2\rangle$ 0.5% $\vert +15/2\rangle$ 0.1% $\vert -15/2\rangle$				43.5% $\vert +13/2\rangle$ 18.7% $\vert -13/2\rangle$ 11.2% $\vert +9/2\rangle$ 6.1% $\vert +5/2\rangle$ 5.2% $\vert -9/2\rangle$ 4.1% $\vert +7/2\rangle$ 3.3% $\vert -5/2\rangle$ 2.0% $\vert -1/2\rangle$ 1.9% $\vert +3/2\rangle$ 1.5% $\vert +1/2\rangle$ 0.9% $\vert +11/2\rangle$ 0.6% $\vert +15/2\rangle$ 0.4% $\vert -3/2\rangle$ 0.2% $\vert -7/2\rangle$ 0.1% $\vert -15/2\rangle$			

Table S9 The comparison of the experimental and theoretical (using the *ab initio* method, shown in respect to the experimental position of the ground Kramers doublet) energies (cm^{-1}) of emission components of the band related to the $^4F_{9/2} \rightarrow {}^6H_{15/2}$ electronic transition occurring for Dy^{III} complexes of **1** and **2**. The related graphical presentation is given in Fig. 5.

1		**2**	
experimental[a]	*ab initio*	experimental	*ab initio*
21182	21182	21357	-
21001	21003	21191	21191
20867	20884	20987	21052
20806	20853	20889	20947
20720	20807	20832	20871
20701	20777	20753	20815
20695	20751	20697	20714
20589	20662	20632	20699
		20516	20674

a) experimental energy values were obtained as the energy for the centres of Gaussian curves fitted to the emission spectra

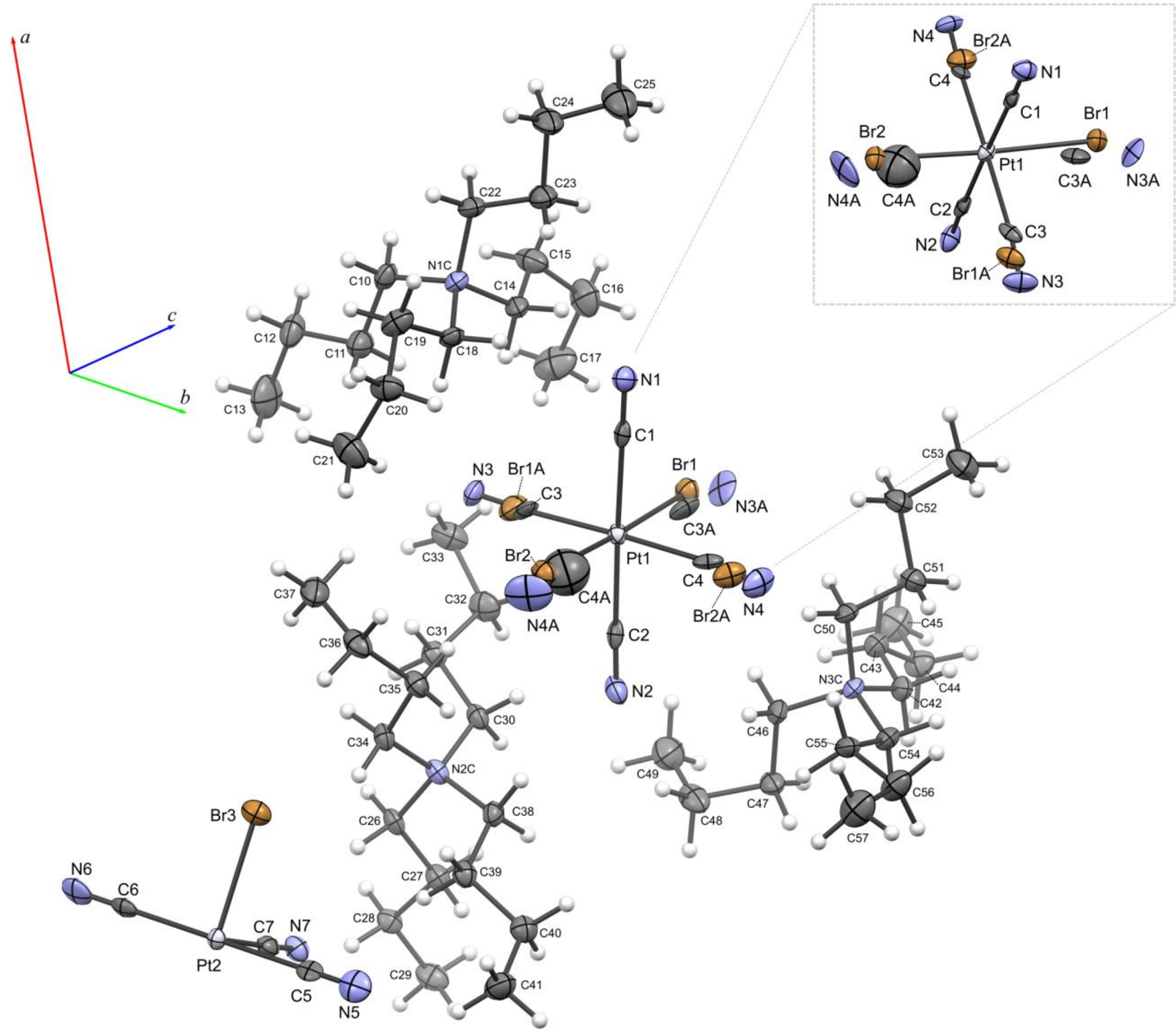

Fig. S14 Asymmetric unit of the crustal structure of $(TBA)_2[PtBr_2(CN)_4]$. The asymmetric unit contains one and one half of $[Pt^{IV}Br_2(CN)_4]^{2-}$ anions in two symmetry-independent positions, as well as three symmetry-independent tetrabutylammonium cations. One of the anions (Pt2) occupies a special position with the metal centre and two opposite CN^- ligands placed on a 2-fold axis. The other $[Pt^{IV}Br_2(CN)_4]^{2-}$ anion occupies a general position and it is affected by positional disorder (inset). The disorder has two components which are related to each other by a 90°-rotation around complex's axis designated by the C1–Pt1–C2 atoms.

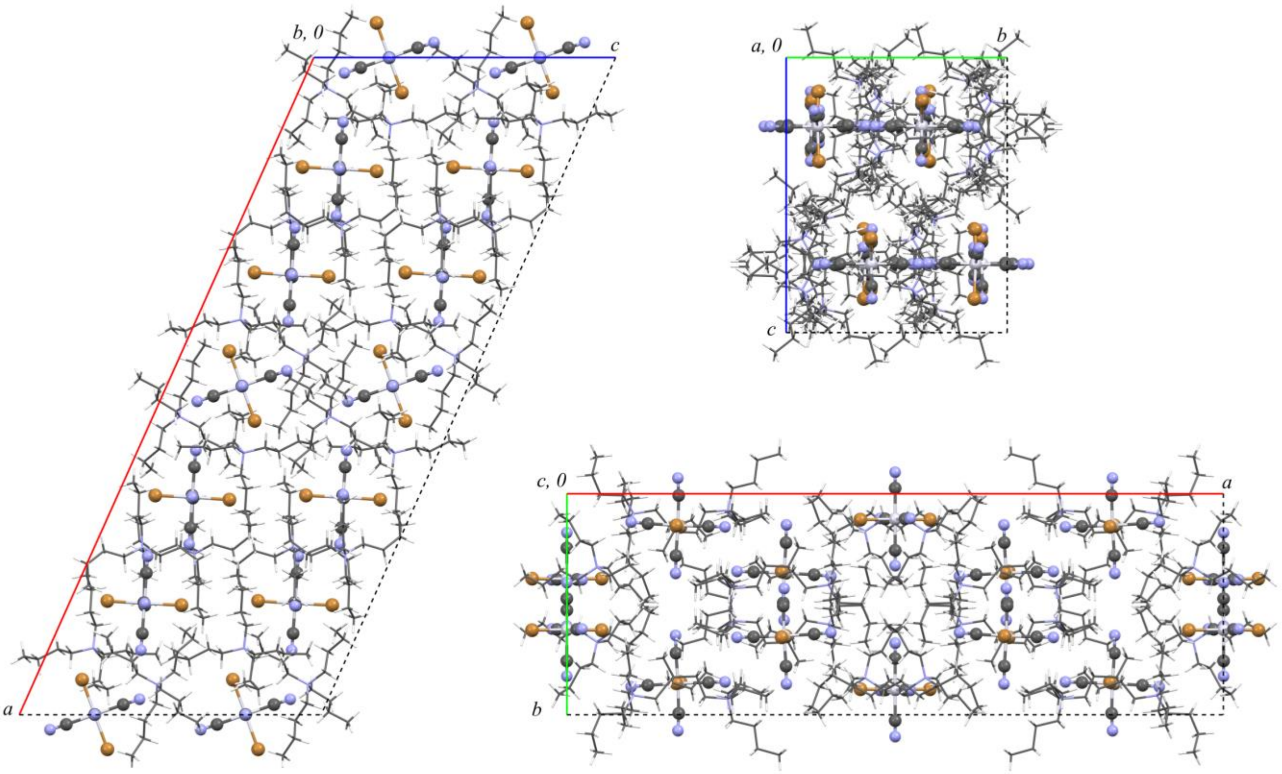

Fig. S15 Packing diagrams for the crystal structure of $(TBA)_2[PtBr_2(CN)_4]$ visualized from the direction of the *a*, *b* and *c* crystallographic axes.

References to Supplementary Information

1. G. Cavallo, P. Metrangolo, R. Milani, T. Pilati, A. Priimagi, G. Resnati and G. Terraneo, *Chem. Rev.*, 2016, **116**, 2478–2601.
2. G. R. Desiraju and R. Parthasarathy, *J. Am. Chem. Soc.*, 1989, **111**, 8725–8726.
3. C. V. Topping and S. J. Blundell, *J. Phys. Condens. Matter*, 2018, **31**, 013001.